

Intra- and interband Raman scattering by free carriers in heavily doped *p*-Si

M. Chandrasekhar,* U. Rössler,[†] and M. Cardona

Max-Planck-Institut für Festkörperforschung, Stuttgart, Federal Republic of Germany

(Received 1 February 1980)

Raman scattering from the free carriers in *p*-Si has been studied at high doping levels ($p = 1.5 \times 10^{19}$ cm^{-3} and 1.5×10^{20} cm^{-3}). The features observed in the Raman spectra at low frequency are similar to those for *n*-Si: a strong tail which can be seen only in $\Gamma_{25'}$ scattering symmetry. A theory of the Raman cross section is formulated and it is found that this tail is due to fluctuations of the effective mass of the free carriers in the warped upper valence band. The observed selection rule can be accounted for. For the more lightly doped samples (1.5×10^{19} cm^{-3}) the dependence of the Raman spectra on uniaxial stress in the [111] and [100] directions and on the exciting frequency has been studied. It can be explained in terms of the stress-dependent band structure of Si and the frequency-dependent interaction for the scattering process, respectively. Superimposed on the intraband tail a hump is also found, whose spectral position varies for lower stress as the stress-dependent splitting of the topmost valence bands. Therefore this hump is attributed to interband transitions. At higher stresses the hump gets pinned at a frequency of about 400 cm^{-1} . This feature cannot be understood in terms of the stress-dependent band structure.

I. INTRODUCTION

Heavy doping in Si is known to produce free carriers whose excitation can be observed in Raman scattering.¹ Interband transitions between valence^{2,3} or conduction^{4,5} bands are of sufficiently low frequency to interfere with the zone-center optic phonon and produce Fano-type asymmetric line shapes. Intraband scattering is usually screened in an isotropic plasma but can be observed both in *n*- and *p*-Si (Refs. 6–8) due to the multivalley nature of the conduction band and the complex warped valence bands, respectively. In the Raman spectrum this intraband scattering takes the form of a broad low-frequency tail in both *n*- and *p*-Si. We have studied this low-frequency tail in *p*-Si for high hole concentrations ($p = 1.5 \times 10^{19}$ and 1.5×10^{20} cm^{-3}). The most detailed study was performed for the lower concentration where we investigated the selection rules for a number of polarization configurations, its behavior under uniaxial stress along the [001] and [111] directions, and the dependence of its intensity on exciting frequency and carrier concentration. Existing theories for the Raman cross section, which are restricted to the multivalley case⁹ or to nonparabolic bands,¹⁰ are generalized for a plasma with carriers in an energy band with arbitrary dispersion. It turns out that the warping, as well as either the multivalley structure or nonparabolicities, gives rise to unscreened Raman scattering. This extended theory successfully explains several of the observed features, such as the selection rules, the dependence on the exciting frequency, and the dependence on uniaxial stress.

When a uniaxial stress is applied we also observe a broad hump superimposed on the intraband tail

due to interband scattering. This hump is not seen without stress in the more lightly doped sample. With increasing stress the frequency of this hump follows the splitting of the valence bands under stress for low stresses but becomes pinned at about 400 cm^{-1} for high stresses. No satisfactory explanation has been found for this effect.

Section II is a short survey of the experimental details. The theory is presented in Sec. III, while Sec. IV deals with the experimental results and their interpretation.

II. EXPERIMENTAL DETAILS

Raman spectra were taken at room temperature using the back-scattering geometry standard for opaque samples. Spectra Physics Ar⁺ and Kr⁺ lasers were used to provide the exciting radiation. All measurements under uniaxial stress were done using 400–600 mW of 6471-Å radiation from a Kr⁺ laser. A Spex-triple or Spex-double monochromator with holographic gratings and a cooled photomultiplier equipped with photon counting electronics were used for detection. The data were stored on a multichannel analyzer. Counting times from 5 to 50 sec were used, the longer counting times for polarization parallel to the slit in the red region where the grating efficiency was poor. The stress apparatus used, provided with digital readout, has been described in the literature.¹¹ Typical compressive stress up to 20 kbar could be reached.

Samples were cut from single crystals of Si and x-ray oriented to within 1°. Typical dimensions were $20 \times 1.3 \times 1.3$ mm^3 , the stress applied along the long dimension. The face used for Raman scattering was polished to optical flatness with

0.3 μm alumina and polish-etched with Syton for 10 min. Care was taken to minimize fine hairline scratches and hence Rayleigh scattering, in order to make measurements of the inelastic tail reliable. The carrier concentrations of the samples as quoted were determined by measuring the resistivity with a four-probe technique. The relationship between resistivity and electron concentration was taken from Ref. 12.

III. THEORY OF THE SCATTERING CROSS SECTION

The theory of light scattering from solid-state plasmas has been reviewed recently.^{13,14} In particular, the Raman cross section has been derived for n -doped material to describe scattering due to intervalley fluctuations,⁹ nonparabolicity of the conduction band,¹⁰ and spin-density fluctuations.^{15,16} For p -doped material the scattering cross section has been formulated for the interband process.¹⁷ In the following we generalize the existing theory by deriving an expression for the Raman cross section, which is valid for both inter- and intra-band scattering from carriers in an arbitrarily shaped energy band.

$$\mathcal{F}_{\nu\nu'}(\vec{k}, 0) = \frac{e^2}{2c^2} \vec{A}_1 \left[\frac{1}{m} \delta_{\nu\nu'} + \frac{1}{m^2} \sum_n \left(\frac{\langle \nu\vec{k} | \vec{p} | n\vec{k} \rangle \langle n\vec{k} | \vec{p} | \nu'\vec{k} \rangle}{E_\nu(\vec{k}) - E_n(\vec{k}) - \hbar\omega_2} + \frac{\langle n\vec{k} | \vec{p} | \nu'\vec{k} \rangle \langle \nu\vec{k} | \vec{p} | n\vec{k} \rangle}{E_\nu(\vec{k}) - E_n(\vec{k}) + \hbar\omega_1} \right) \right] \vec{A}_2^* \quad (3)$$

where \vec{A}_1 , ω_1 (\vec{A}_2 , ω_2) are the vector potential and frequency of the incident (scattered) light. If $\hbar\omega_1$, $\hbar\omega_2$ are small compared with the energy gaps $E_\nu(\vec{k}) - E_n(\vec{k})$, the dyadic expression in the large square brackets represents the generalization of the inverse mass tensor. If in particular ν, ν' refer to the different states of the topmost valence band in Si (Γ_8^+ symmetry), the large square bracket becomes the Luttinger matrix,¹⁸ while for an energy band of arbitrary dispersion it is the \vec{k} -dependent inverse mass tensor.

In order to calculate the response of the many-particle system [Eq. (1)] to the external perturbation [Eq. (2)] we proceed along the lines of previous work.¹⁰ The scattering cross section is expressed by the correlation function of H_{int} which via the dissipation-fluctuation theorem can be related to the Green's function

$$G(\vec{q}, t) = \sum_{\substack{\vec{k}, \vec{k}' \\ \nu, \nu', \mu, \mu'}} \mathcal{F}_{\nu\nu'}^*(\vec{k}, \vec{q}) \mathcal{F}_{\mu\mu'}(\vec{k}', \vec{q}) \times \mathcal{S}_{\nu'\nu\mu\mu'}(\vec{k}, \vec{k}', \vec{q}, t), \quad (4)$$

where

The Hamiltonian for the solid-state plasma reads

$$H_0 = \sum_{\nu\vec{k}} E_\nu(\vec{k}) c_{\nu\vec{k}}^\dagger c_{\nu\vec{k}} + \frac{1}{2} \sum_{\nu\nu', \vec{k}\vec{k}', \vec{q}} \frac{4\pi e^2}{\epsilon_0 q^2} c_{\nu'\vec{k}'+\vec{q}}^\dagger c_{\nu\vec{k}-\vec{q}}^\dagger c_{\nu'\vec{k}'} c_{\nu\vec{k}}, \quad (1)$$

where $E_\nu(\vec{k})$ is the energy band and $c_{\nu\vec{k}}$ denotes the annihilation operator for a carrier in the ν th band of wave vector \vec{k} . The second term in Eq. (1) describes the Coulomb interaction between the carriers screened by the dielectric constant ϵ_0 of the semiconductor. The sum over ν includes only energy bands which contain the carriers of the plasma, i.e., for p -Si the upper valence bands. The interaction with the radiation field can be formulated as

$$H_{\text{int}} = \sum_{\nu\nu', \vec{k}} \mathcal{F}_{\nu\nu'}(\vec{k}, \vec{q}) c_{\nu\vec{k}+\vec{q}}^\dagger c_{\nu'\vec{k}} \quad (2)$$

and describes interband transitions if ν, ν' refer to different bands ($\nu \neq \nu'$), while intraband transitions correspond to $\nu = \nu'$. From Eq. (3.3) of Ref. 16 we obtain in the long-wavelength limit ($q \rightarrow 0$) the expression

$$\mathcal{S}_{\nu'\nu\mu\mu'}(\vec{k}, \vec{k}', \vec{q}, t) = -i\Theta(t) \langle [c_{\nu'\vec{k}-\vec{q}}^\dagger(t) c_{\nu\vec{k}}(t), c_{\mu\vec{k}'}^\dagger(0) c_{\mu\vec{k}}(0)] \rangle. \quad (5)$$

$\Theta(t)$ is the unit step function, $c_{\nu\vec{k}}(t)$ is the time-dependent Fermi operator

$$c_{\nu\vec{k}}(t) = e^{iH_0 t} c_{\nu\vec{k}}(0) e^{-iH_0 t}$$

and the brackets $\langle \rangle$ represent the thermal average. We set up the equation of motion for $\mathcal{S}_{\nu'\nu\mu\mu'}(\vec{k}, \vec{k}', \vec{q})$ and solve it in random-phase approximation (cf. Ref. 10). In the following we consider the Fourier transform $G(\vec{q}, \omega)$ of Eq. 4.

A. Intraband scattering

For intraband transition ($\nu = \nu'$) we obtain a formula which is a generalization of Wolff's result¹⁰ for a nonparabolic band:

$$G_{\text{intra}}(\vec{q}, \omega) = -\frac{1}{2\pi} \frac{L_2(\vec{q}, \omega)}{1 + (4\pi e^2/\epsilon_0 q^2) L_0(\vec{q}, \omega)} + \frac{1}{2\pi} \frac{4\pi e^2}{\epsilon_0 q^2} \frac{L_1^2(\vec{q}, \omega) - L_0(\vec{q}, \omega) L_2(\vec{q}, \omega)}{1 + (4\pi e^2/\epsilon_0 q^2) L_0(\vec{q}, \omega)}, \quad (6)$$

where

$$L_{\alpha}(\vec{q}, \omega) = - \sum_{\vec{k}, \nu} \mathcal{F}_{\nu\nu}^{\alpha}(\vec{k}, 0) \times \frac{f_{\nu, \vec{k}-\vec{q}} - f_{\nu, \vec{k}}}{\hbar\omega - E_{\nu}(\vec{k}) + E_{\nu}(\vec{k}-\vec{q})}, \quad (7)$$

$f_{\nu\vec{k}}$ being the Fermi distribution function. For $\alpha=0$ Eq. (7) represents the contribution of the carriers to the polarizability. In this expression we have neglected the effect of impurity scattering, which for n -Si was considered in Ref. 7 and later neglected on account of the observed experimental facts. Later on we shall describe the polarizability in the Drude model and consider only its dependence on the carrier concentration.

From the discussion of Eq. (3) it is clear that these results are valid for energy bands of arbitrary dispersion; the sum over ν considers the different parts of a multiply connected energy contour as, e.g., in the multivalley case of n -Si. If we consider intraband transitions in p -Si, e.g., scattering within the topmost valence subband, the sum over ν is redundant and shall be dropped. Using the identity

$$\mathcal{F}(\vec{k})\mathcal{F}(\vec{k}') = -\frac{1}{2} \{ [\mathcal{F}(\vec{k}) - \mathcal{F}(\vec{k}')]^2 - \mathcal{F}^2(\vec{k}) - \mathcal{F}^2(\vec{k}') \},$$

$$G_{\text{intra}}(\vec{q} \rightarrow 0, \omega) = \frac{1}{2\pi} \sum_{\vec{k}, \vec{k}'} [\mathcal{F}(\vec{k}) - \mathcal{F}(\vec{k}')]^2 g(\vec{k}, \vec{q}) g(\vec{k}', \vec{q}) / \sum_{\vec{k}} g(\vec{k}, \vec{q}). \quad (9)$$

We finally obtain the Raman cross section for intraband scattering

$$\left. \frac{\partial^2 R}{\partial \omega \partial \Omega} \right|_{\text{intra}} = (1 + n_{\omega}) \text{Im} [G_{\text{intra}}(\vec{q}, \omega)], \quad (10)$$

where n_{ω} is the Bose factor.

We see from Eq. (9) that intraband Raman scattering from a solid-state plasma is due to deviations of the energy band from the parabolic and isotropic case, for which $\mathcal{F}(\vec{k}) = \mathcal{F}(\vec{k}') = \text{constant}$ for arbitrary \vec{k}, \vec{k}' . Thus nonparabolicity and warping, or else the wave-vector dependence of the effective carrier masses, cause the intraband Raman scattering at low frequencies.

B. Interband scattering

For interband scattering we have to consider Eqs. (4) and (5) for $\nu \neq \nu'$ and $\mu \neq \mu'$ and obtain from the equation of motion

$$S_{\nu'\nu\mu\mu'}(\vec{k}, \vec{k}', \vec{q}) = \frac{1}{2\pi} \delta_{\mu\nu} \delta_{\mu'\nu'} \delta_{\vec{k}\vec{k}'} \times \frac{f_{\nu', \vec{k}-\vec{q}} - f_{\nu, \vec{k}}}{\hbar\omega - E_{\nu}(\vec{k}) + E_{\nu'}(\vec{k}-\vec{q})} \quad (11)$$

and the Green's function

we obtain from Eq. (6)

$$G_{\text{intra}}(\vec{q}, \omega) = \frac{1}{2\pi\epsilon(\vec{q}, \omega)} \left(\sum_{\vec{k}} \mathcal{F}^2(\vec{k}) g(\vec{k}, \vec{q}) - \phi \sum_{\vec{k}, \vec{k}'} [\mathcal{F}(\vec{k}) - \mathcal{F}(\vec{k}')]^2 \times g(\vec{k}, \vec{q}) g(\vec{k}', \vec{q}) \right), \quad (8)$$

where

$$\phi = \frac{4\pi e^2}{\epsilon_0 q^2}, \quad g(\vec{k}, \vec{q}) = \frac{f_{\vec{k}-\vec{q}} - f_{\vec{k}}}{\hbar\omega - E(\vec{k}) + E(\vec{k}-\vec{q})}$$

and

$$\epsilon(\vec{q}, \omega) = 1 - \phi \sum_{\vec{k}} g(\vec{k}, \vec{q})$$

is the dielectric function of the free carriers, which diverges for q and ω tending to zero. Therefore, the first term of Eq. (8) vanishes in the long-wavelength limit, due to screening, and for the second term, however, the divergence in $\epsilon(q, \omega)$ can be compensated by the factor ϕ for $q \rightarrow 0$. In this case the dominant contribution to G_{intra} is given by

$$G_{\text{inter}}(\vec{q}, \omega) = -\frac{1}{2\pi} \sum_{\nu\nu'} |\mathcal{F}_{\nu\nu'}(\vec{k}, \vec{q})|^2 \times \frac{f_{\nu', \vec{k}-\vec{q}} - f_{\nu, \vec{k}}}{\hbar\omega - E_{\nu}(\vec{k}) + E_{\nu'}(\vec{k}-\vec{q})}. \quad (12)$$

We see from Eq. (3) that interband scattering is possible only via virtual transitions to higher and from lower bands.¹⁷

C. Approximations for intraband scattering

Starting from Eq. (3) we realize that the Raman cross section [Eq. (10)] is obtained from a fourth-rank tensor contracted with the polarization vectors of incident and scattered light (twice each). Since a numerical calculation of the tensor components is a difficult project, we try to formulate them in an approximate way. For this purpose we divide the hole plasma into components in such a way that all carriers belonging to a particular plasma component have the same \vec{k} -dependent mass tensor. While for n -Si this decomposition is exactly possible due to the multivalley structure, we will see in the next section that the valence band structure of Si suggests an approximate de-

composition, also for p -doped material. We assume that all carriers of a plasma component occupy the Bloch states in a simply connected volume of \vec{k} space. With these specifications we can rewrite Eq. (7) as

$$L_\alpha(\vec{q}, \omega) \simeq \sum_\nu \mathfrak{F}_{\nu\nu}^\alpha \sum_{\vec{k}} \frac{f_{\nu, \vec{k}-\vec{q}} - f_{\nu, \vec{k}}}{\hbar\omega - E_\nu(\vec{k}) + E_\nu(\vec{k}-\vec{q})}, \quad (13)$$

where ν now refers to the different plasma components;

$$\mathfrak{F}_{\nu\nu} = \frac{2\pi\hbar c}{(\omega_1\omega_2)^{1/2}} \vec{e}_1 \cdot \frac{1}{m_\nu^*} \cdot \vec{e}_2 \quad (14)$$

is essentially the inverse mass tensor of the carriers in the ν th component contracted with the

$$T_{ij\alpha\beta} = \sum_\nu \left(\frac{1}{m_\nu^*} \right)_{ij} F_\nu \sum_{\nu'} \left(\frac{1}{m_{\nu'}^*} \right)_{\alpha\beta} F_{\nu'} / \sum_\nu F_\nu - \sum_\nu \left(\frac{1}{m_\nu^*} \right)_{ij} \left(\frac{1}{m_\nu^*} \right)_{\alpha\beta} F_\nu. \quad (17)$$

In this form we will be able to discuss the polarization dependence and the selection rules of the intraband scattering (Sec. IV A) and the dependence of the scattering intensity on the carrier concentration (Sec. IV E).

IV. DISCUSSION AND EXPERIMENTAL RESULTS

A. Selection rules

A low-frequency tail extending from near zero to about 400 cm^{-1} is observed in the $\Gamma_{25'}$ scattering geometry. We have compared the intensity of the tail for the sample with $1.5 \times 10^{19} \text{ cm}^{-3}$ carriers at several fixed Raman frequencies with that of the peak intensity of the zone center optical phonon (known to have $\Gamma_{25'}$ symmetry). We find the intensity ratio a constant [e.g., $(2.50 \pm 0.6) \times 10^{-2}$ at 20 cm^{-1}] for the 10 different polarization configurations used. We thus conclude that the intraband scattering has $\Gamma_{25'}$ symmetry. Using the noise in the experimental data at 20 cm^{-1} as the limiting factor we infer that the intensity of the tail in either Γ_1 or Γ_{12} symmetry is a factor of six or more weaker than in $\Gamma_{25'}$ symmetry for the sample with $p = 1.5 \times 10^{19} \text{ cm}^{-3}$ (Fig. 1).

From Eq. (9) we know that the strength of the intraband scattering is determined by the deviation of the energy band from isotropy and parabolicity. In the valence bands of Si the heavy hole band, which has about ten times as many carriers as the light hole band, is strongly warped. We therefore attempt to explain the observed low-frequency tail only with intraband scattering within the heavy hole band. A typical constant energy contour of the heavy hole band as calculated from a 6×6 Luttinger matrix (including the interaction

polarization vectors \vec{e}_1 and \vec{e}_2 of incident and scattered light. The \vec{k} sum in Eq. (13) defines the contribution of the ν th plasma component to the polarizability of the free carriers

$$F_\nu(\vec{q}, \omega) = \sum_{\vec{k}} \frac{f_{\nu, \vec{k}-\vec{q}} - f_{\nu, \vec{k}}}{\hbar\omega - E_\nu(\vec{k}) + E_\nu(\vec{k}-\vec{q})}. \quad (15)$$

Starting from Eq. (6) we obtain the Raman cross section for intraband scattering in the long-wavelength limit:

$$\frac{\partial^2 R}{\partial \omega \partial \Omega} = (1 + n_\omega) \frac{1}{2\pi} \frac{\text{Im}(L_1^* L_0 - |L_0|^2 L_2)}{|L_0|^2} \sim \sum_{ij\alpha\beta} e_{1i} e_{1j} e_{2\alpha} e_{2\beta} T_{ij\alpha\beta}, \quad (16)$$

where

with the split-off band) is shown in Fig. 2. The band parameters used were $\gamma_1 = 4.285$, $\gamma_2 = 0.339$, $\gamma_3 = 1.446$ and $\Delta_{so} = 44 \text{ meV}$.¹⁹ The strong deviation from spherical energy contours (warping) is due to the large difference between γ_2 and γ_3 . The dominant features of the surface of constant energy, irrespective of the value of this energy, are the strong lobes in the $\langle 110 \rangle$ directions. We assume in the following calculations that the plasma can be divided into one component consisting of all carriers in a spherical central region of radius k_s around the zone center and 12 components with the carriers in these lobes. We further assume that, due to scattering by the impurities, the wave vector \vec{k} loses the property as a good quantum number to such an extent that in the central region all particles can be considered to have equal isotropic mass, whereas in the 12 lobes, a mass anisotropy still persists. With these assumptions we calculate the scattering cross section by evaluating the tensor components $T_{ij\alpha\beta}$ of Eq. (17). As can be seen from Eq. (17), $T_{ij\alpha\beta}$ is related to the tensor of the inverse effective mass which for the $[110]$ lobe is

$$\left(\frac{m}{m^*} \right)_{[110]} = \begin{bmatrix} \epsilon_{110} & \gamma_{110} & 0 \\ \gamma_{110} & \epsilon_{110} & 0 \\ 0 & 0 & \delta_{110} \end{bmatrix}, \quad (18)$$

where m is the free electron mass. This expression follows from the symmetry of the $[110]$ direction if we assume the same mass tensor for all carriers in the lobe. We decompose the mass tensor in terms of the three Raman tensors²⁰ Γ_1 , Γ_{12} , and $\Gamma_{25'}$.

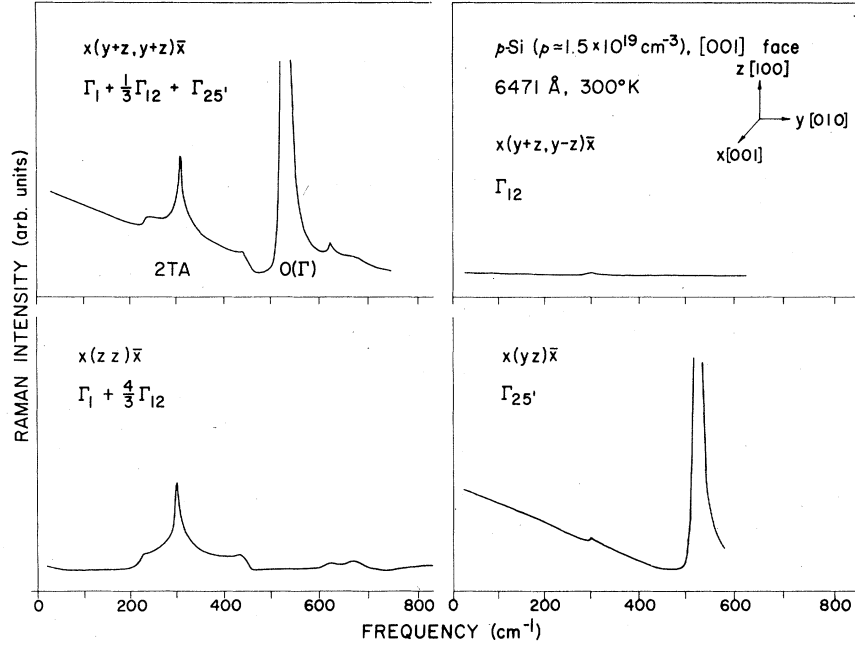


FIG. 1. Raman spectra for p -Si ($p = 1.5 \times 10^{19} \text{ cm}^{-3}$) for four different polarization configurations. The low-frequency tail appears only in the scattering geometries which contain the $\Gamma_{25'}$ component of the Raman tensor.

$$\left(\frac{m}{m^*}\right)_{\langle 110 \rangle} = \begin{pmatrix} a & 0 & 0 \\ 0 & a & 0 \\ 0 & 0 & a \end{pmatrix} + \begin{pmatrix} b & 0 & 0 \\ 0 & b & 0 \\ 0 & 0 & -2b \end{pmatrix} + \begin{pmatrix} 0 & d & 0 \\ 0 & 0 & 0 \\ 0 & 0 & 0 \end{pmatrix}, \quad (19)$$

where

$$a = \frac{1}{3}(2\epsilon_{110} + \delta_{110}), \quad b = \frac{1}{3}(\epsilon_{110} - \delta_{110}), \quad d = \gamma_{110}.$$

The contribution of different $\langle 110 \rangle$ lobes to T_{ifab} can be found in Table I.

In order to consider the polarizability factor F_ν in evaluating Eq. (17), we use the Drude theory according to which $F_\nu \sim n_\nu$, where n_ν is the carrier density in the ν th plasma component. A calculation for zero temperature yields for $p = 1.5 \times 10^{19} \text{ cm}^{-3}$ and an average heavy hole mass of $0.52m_0$ a

carrier density $n_0 = 3.5 \times 10^{17} \text{ cm}^{-3}$ in the central region [$k_x = 0.04(2\pi/a)$]. For finite temperatures a larger number of states outside the central region will be occupied at the expense of states inside the central region; thus the value of n_0 given above can be regarded as an upper bound of the actual carrier density in the central region. The carrier density in cm^{-3} for each of the $\langle 110 \rangle$ lobes is thus at least

$$n_{110} = \frac{1}{12}(1.5 \times 10^{19} - 3.5 \times 10^{17}) \approx 1.22 \times 10^{18} \text{ cm}^{-3}.$$

The nonvanishing tensor components of Eq. (17) are obtained by using Table I:

TABLE I. Cartesian components of inverse mass tensor for the different $\langle 110 \rangle$ lobes.

Lobe	$\left(\frac{m}{m^*}\right)_{xy}$	$\left(\frac{m}{m^*}\right)_{yz}$	$\left(\frac{m}{m^*}\right)_{zx}$	$\left(\frac{m}{m^*}\right)_{xx}$	$\left(\frac{m}{m^*}\right)_{yy}$	$\left(\frac{m}{m^*}\right)_{zz}$
[110]	γ_{110}	0	0	ϵ_{110}	ϵ_{110}	δ_{110}
[110]	γ_{110}	0	0	ϵ_{110}	ϵ_{110}	δ_{110}
[110]	$-\gamma_{110}$	0	0	ϵ_{110}	ϵ_{110}	δ_{110}
[110]	$-\gamma_{110}$	0	0	ϵ_{110}	ϵ_{110}	δ_{110}
[101]	0	0	γ_{110}	ϵ_{110}	δ_{110}	ϵ_{110}
[101]	0	0	γ_{110}	ϵ_{110}	δ_{110}	ϵ_{110}
[101]	0	0	$-\gamma_{110}$	ϵ_{110}	δ_{110}	ϵ_{110}
[101]	0	0	$-\gamma_{110}$	ϵ_{110}	δ_{110}	ϵ_{110}
[011]	0	γ_{110}	0	δ_{110}	ϵ_{110}	ϵ_{110}
[011]	0	γ_{110}	0	δ_{110}	ϵ_{110}	ϵ_{110}
[011]	0	$-\gamma_{110}$	0	δ_{110}	ϵ_{110}	ϵ_{110}
[011]	0	$-\gamma_{110}$	0	δ_{110}	ϵ_{110}	ϵ_{110}

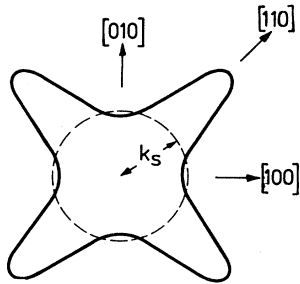


FIG. 2. Characteristic contour of constant energy of the topmost valence subband.

$$\begin{aligned}
T_{xxxx} &= [\epsilon_{000}n_0 + (4\delta_{110} + 8\epsilon_{110})n_{110}]^2/n_{tot} \\
&\quad - [\epsilon_{000}^2n_0 + (4\delta_{110}^2 + 8\epsilon_{110}^2)n_{110}] \\
&= T_{yyyy} = T_{zzzz}, \\
T_{xxyy} &= [\epsilon_{000}n_0 + (4\delta_{110} + 8\epsilon_{110})n_{110}]^2/n_{tot} \\
&\quad - [\epsilon_{000}^2n_0 + (8\epsilon_{110}\delta_{110} + 4\epsilon_{110}^2)n_{110}] \\
&= T_{xxzz} = T_{yyzz} = T_{yyxx} = T_{zzyy} = T_{zzxx}, \quad (20) \\
T_{xyxy} &= -4\gamma_{110}^2n_{110} \\
&= T_{yxxy} = T_{xxyx} = T_{yxyx} = T_{xyxx} = T_{xxxy},
\end{aligned}$$

where $n_{tot} = n_0 + 12n_{110} = p$. The inverse average heavy hole mass is, in our case, $\epsilon_{000} = 1/0.52$. The remaining mass parameters were calculated numerically from the eigenvalues of a 6×6 Luttinger matrix. We obtain for $\vec{k} = (k, k, 0)/\sqrt{2}$

$$\epsilon_{110} = 4.25, \quad \delta_{110} = 3.5, \quad \gamma_{110} = -4.2$$

almost independent of k . Thus the numerical results support the assumption made above by attributing the same inverse mass tensor to all carriers in the $\langle 110 \rangle$ lobes. From these numbers we calculate finally the ratio

$$\begin{aligned}
T_{xxxx} : T_{xxyy} : T_{xyxy} &= 5:1:120, \\
p &= 1.5 \times 10^{19} \text{ cm}^{-3}.
\end{aligned} \quad (21)$$

Using Eq. (19) the components T_{ijab} can be readily identified in terms of the second rank Raman tensors: T_{xxxx} and T_{xxyy} are combinations of Γ_1 and Γ_{12} while T_{xyxy} is $\Gamma_{25'}$. The allowed scattering configuration for interband scattering is therefore $\Gamma_{25'}$; it is 24 times as intense as Γ_1 and Γ_{12} according to this calculation.²¹

B. Behavior under stress

Raman spectra as a function of uniaxial stress along the $[001]$ and $[111]$ crystal directions are shown in Figs. 3 and 4 for p -Si ($p = 1.5 \times 10^{19} \text{ cm}^{-3}$) at room temperature. Comparing the spectra for zero (solid lines) and high stress (15 kbar, dashed lines) for either stress direction we see that the intensity of the tail decreases with increasing stress. This is expected, since the upper valence bands split under uniaxial stress, the warping of the topmost sub-band vanishes and the energy contour becomes ellipsoidal. Thus at high stresses we are left with a single component plasma with equal (anisotropic) mass for all carriers which does not contribute to the unscreened Raman cross section [of Eq. (9)]. The increase of the Raman intensity in the $x(yz)\bar{x}$ configuration at 5.5 kbar (Fig. 3) and 6 kbar (Fig. 4) can be attributed to interband scattering (see below).

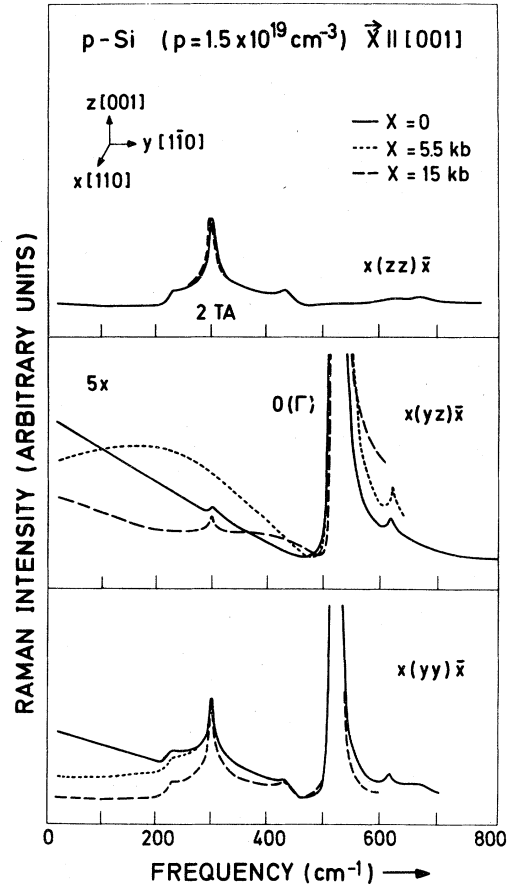


FIG. 3. Stress dependence of Raman spectra of p -Si ($p = 1.5 \times 10^{19} \text{ cm}^{-3}$) for uniaxial stress along $[001]$ at room temperature.

At low stress (dotted lines) we see a small decrease in the intensity of the tail for the $x(yy)\bar{x}$ configuration for both stress directions, indicative of the vanishing of the interband scattering at high stress. In the $x(zz)\bar{x}$ configuration for $[111]$ stress (Fig. 4) the tail increases in intensity for low stress and then decreases for high stress. This behavior is possibly due to the fact that the twelve $[110]$ lobes become inequivalent under $[111]$ stress. The stress-dependent band structure indicates an increase of k_F for the $[1\bar{1}0]$ directions and a decrease of k_F for the $[110]$ directions. Thus we expect a redistribution of carriers among the different plasma components which for low stress values can lead to an increased scattering efficiency.

C. Interband scattering

Interband scattering between the valence bands is observed in the $x(yz)\bar{x}$ configuration for both stress directions as a hump superimposed on the decreasing intraband scattering tail (Figs. 5 and

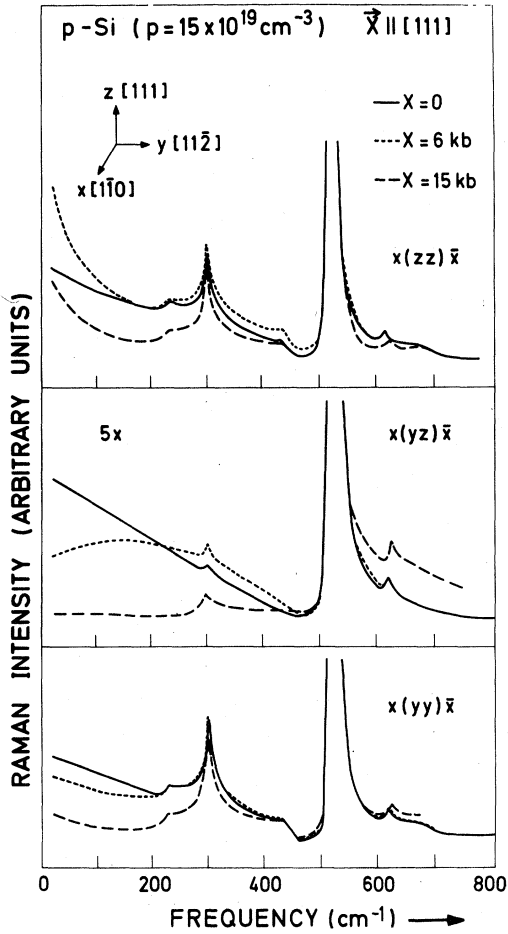


FIG. 4. Stress dependence of Raman spectra of *p*-Si ($p = 1.5 \times 10^{19} \text{ cm}^{-3}$) for uniaxial stress along [111] at room temperature.

6). It is present in the other two scattering configurations, but in these cases is difficult to distinguish from the strong second-order (2TA) scattering. The central frequencies of the hump as a function of stress are plotted in Figs. 7 and 8. For low stresses (up to 8 kbar) the frequency of the hump follows the splitting of the valence bands at $k = 0$ under stress. It also corresponds closely to the calculated maximum of the combined density of states for transitions between these bands (Fig. 7). This fact leads us to ascribe the hump to interband scattering. At stresses higher than 8 kbar the hump tends to be pinned at a frequency of about 400 cm^{-1} and fades away at 18 or 20 kbar. Since this behavior cannot be explained by peculiarities of the stress-dependent band structure we conjecture that the pinning must be due to electron-phonon interaction with optical phonons with wave vectors much larger than \vec{q} (momentum transfer in the scattering process).

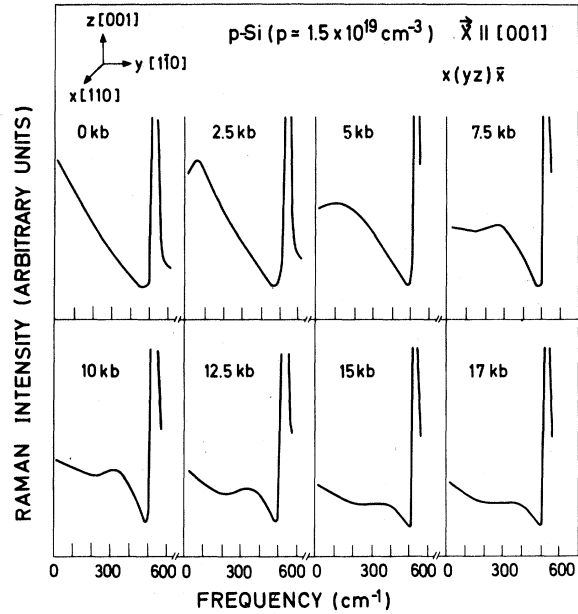


FIG. 5. Stress dependence of Raman spectra for $x(yz)\bar{x}$ polarization and stress along [001].

D. Dependence on exciting energy

We have studied the intraband tail as a function of exciting frequency for several laser lines whose energies ranged from 1.65 to 2.54 eV. A crossed polarization configuration was chosen so that only the tail and the zone-center optical phonon appear.

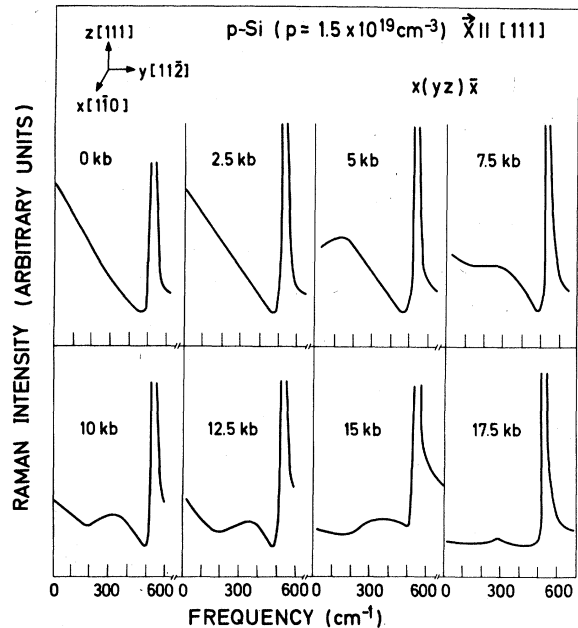


FIG. 6. Stress dependence of Raman spectra for $x(yz)\bar{x}$ polarization and stress along [111].

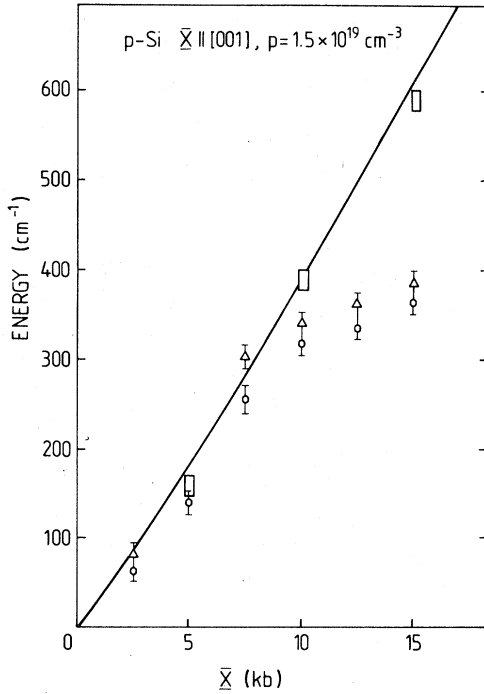


FIG. 7. Position of the hump (circles and triangles) as a function of uniaxial stress along [001]. The circles represent the central frequency of the hump read directly from the spectra, while the triangles are obtained by subtracting the line shape of the tail. The valence-band splitting at $k=0$ (full line) and the position of the maximum of the interband continuum calculated for $T=300$ K (squares) are also given for comparison.

The scattering by optical phonons in this energy range (away from the 3.4-eV E'_0 resonance) should have an ω_L^4 dependence, where ω_L is the exciting laser frequency. The relative intensity of the tail to that of the peak of the optical phonon divided by ω_L^4 is plotted in Fig. 9 for the sample with $p=1.5 \times 10^{19} \text{ cm}^{-3}$. The intensity of the tail was measured at 20, 50, 100, and 150 cm^{-1} . Figure 9 demonstrates a systematic decrease of the tail intensity with increasing frequency. Inspection of the frequency dependence of $\mathcal{F}_{\nu\nu}$ [Eq. (3)] leads us to expect an increase of the scattering efficiency with increasing laser energy (below the E'_0 gap).

More recently, however, the absolute Raman cross section of the phonon has been measured for Si as a function of the exciting laser energy.²² These data demonstrate, besides the off-resonance ω^4 dependence, an increase of the Raman cross section due to resonance enhancement for laser energies used in our experiments. In light of these results the experimental data of Fig. 9 indicate that the resonance enhancement of the phonon process is stronger than that of the intraband scattering.

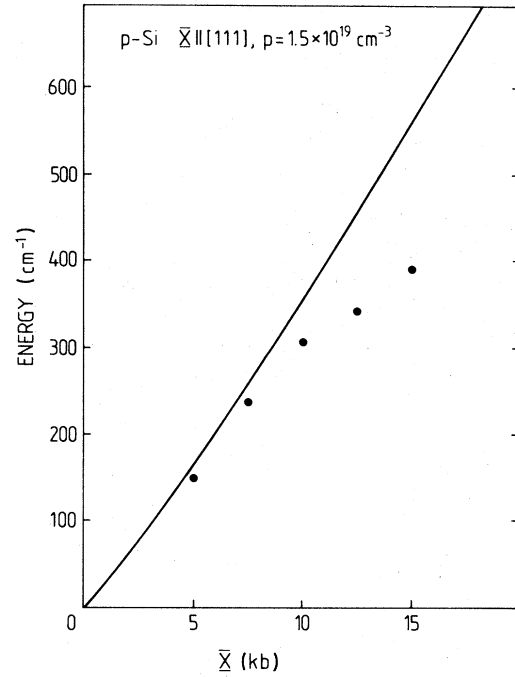


FIG. 8. Position of the hump (circles) as function of uniaxial stress along [111]. The valence-band splitting at $k=0$ (full line) is also given for comparison.

In order to confirm this conjecture we ought to evaluate the frequency dependence of the intraband scattering along the lines of Sec. III C by calculating the frequency dependence of $\mathcal{F}_{\nu\nu}$ [Eq. (3)] for the different plasma components. Since, however, the resonance enhancement of the intraband scattering is caused by shifting the exciting frequency towards the energy gaps occurring in the denominators of Eq. (3), a simplified calculation seems to be appropriate. The main contribution to $\mathcal{F}_{\nu\nu}$ comes from the lowest conduction bands, corresponding to the gaps E_0 and E'_0 at $k=0$ (Ref. 23). Thus the characteristic frequency dependence of the scattering matrix elements is given by

$$\mathcal{F}_{\nu\nu}(\omega) \sim 1 - \frac{E_0 E_p}{E_0^2 - (\hbar\omega)^2} - \frac{E'_0 E'_p}{E_0'^2 - (\hbar\omega)^2}. \quad (22)$$

We used the parameter values (Ref. 23)

$$E_0 = 4.1 \text{ eV}, \quad E_p = 21.6 \text{ eV}$$

$$E'_0 = 3.4 \text{ eV}, \quad E'_p = 14.4 \text{ eV}$$

and divided the values obtained for $|\mathcal{F}_{\nu\nu}(\omega)|^2$ by the phonon Raman intensity of Ref. 22 and normalized it to the value of 0.4 at 1.5 eV in Fig. 9. From Fig. 1 of Ref. 22 we used the mean value between the experimental and the theoretical intensities to obtain the solid line of Fig. 9 which follows the decrease of the observed intensity ratio with increasing exciting energy.

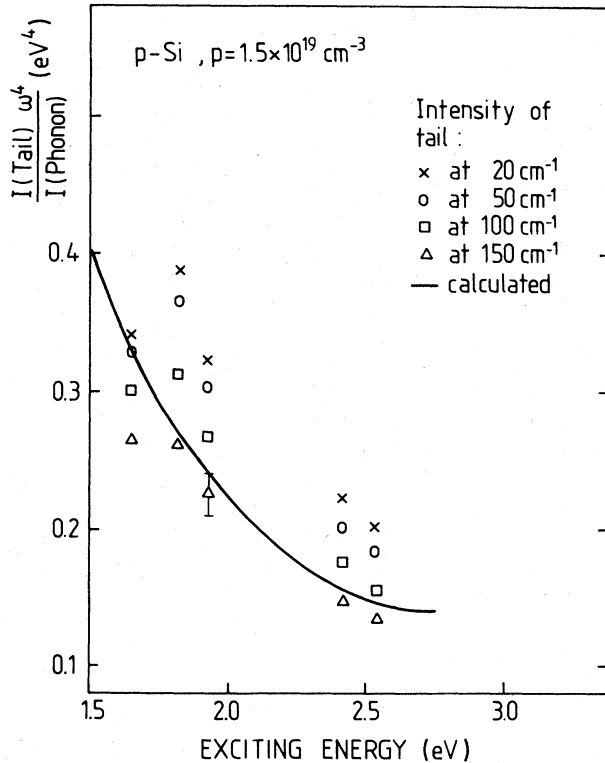


FIG. 9. Dependence of the Raman intensity for intraband scattering on the exciting energy. The calculated curve is obtained by dividing the theoretical values for the tail intensity by the first-order Raman cross section of Ref. 22. (See text).

E. Dependence on carrier concentration

Raman spectra for a sample of $p = 1.5 \times 10^{20} \text{ cm}^{-3}$ taken from a (110) face for three polarizations at zero stress are shown in Fig. 10. The spectra start at 10 cm^{-1} and the quality of the sample surface was not as good as for the more lightly doped samples. Therefore a Rayleigh scattering tail can be seen for the (zz) and (yy) polarizations, which nevertheless is small enough to be unobservable in the crossed (yz) configuration. For (yy) the Rayleigh scattering disappears around 20 cm^{-1} (the point where the slope changes) and for the (zz) at 38 cm^{-1} . In the (zz) spectrum a small leakage of the zone center phonon is also seen, probably due to a slight misalignment. In the (yz) spectrum one can see the hump of interband scattering at zero stress, which was not observable for lower doping.

In comparison with the results for the more lightly doped material we find the same selection rule for the intraband tail: Only the $\Gamma_{25'}$ symmetry is present in the (yy) and (yz) configurations but not in the (zz) configuration (Fig. 10). In order to quantify the observed variation of the tail in-

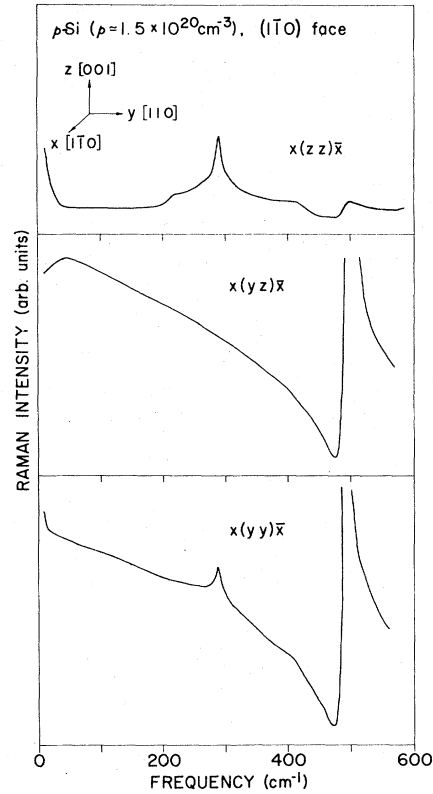


FIG. 10. Raman spectra for $p\text{-Si}$ ($p = 1.5 \times 10^{20} \text{ cm}^{-3}$) for three different polarization configurations.

tensity with the carrier concentration, we compared this intensity to that of the 2TA(X) phonon which appears to remain unchanged with concentration (Table II). It turns out that the efficiency for the intraband scattering increases by a factor of about 5 as the doping is changed from 1.5×10^{19} to $1.5 \times 10^{20} \text{ cm}^{-3}$. Along the lines of Sec. IV A we obtain for the more heavily doped sample with the same normalization as Eq. (21)

$$T_{xxx}:T_{xxy}:T_{xyy} = 34:5:1107,$$

$$p = 1.5 \times 10^{20} \text{ cm}^{-3};$$

thus the calculated intensity ratio is

$$\frac{T_{xxy}(1.5 \times 10^{20} \text{ cm}^{-3})}{T_{xyy}(1.5 \times 10^{19} \text{ cm}^{-3})} = 9,$$

which is in reasonable agreement with the experimental result.

The observation of the interband scattering of zero stress is in accordance with the calculated interband density of states, which as a function of the Raman shift increases more steeply and reaches higher values for $p = 1.5 \times 10^{20} \text{ cm}^{-3}$ than for the more lightly doped material.

TABLE II. Relative intensity of the tail with respect to 2TA(X) scattering of an exciting frequency of 6471 Å for different doping.

Frequency at which tail was measured (cm ⁻¹)	$R = \frac{\text{Intensity of tail}}{\text{Intensity of 2TA(X)}}$		$\frac{R(10^{20})}{R(10^{19})}$
	1.5×10^{19} cm ⁻³	1.5×10^{20} cm ⁻³	
50	0.84	3.93	4.68
100	0.73	3.70	5.07
150	0.60	3.48	5.80

F. Addendum

After this paper had been written a letter reporting a phenomenon similar to that of Fig. 7 appeared.²⁴ In this work the holes are produced in high-purity silicon through optical injection. The "pinning" of Fig. 7 is not seen in this work although only one point is displayed in the region where our pinning occurs. We do not know at this point whether the authors of Ref. 24 tried to observe the pinning or whether the pinning was ab-

sent in their experiment carried out under conditions quite different from ours. A detailed comparison of both types of experiments should help to clarify the nature of the pinning observed by us.

ACKNOWLEDGMENTS

We thank A. Kaiser and G. Fröhlich for polishing and orienting the samples and H. Hirt, P. Wurster, and G. Wolff for technical help.

*Present address: Department of Physics, University of Missouri, Columbia, Missouri 65201.

†Permanent address: Fakultät für Physik, D-8400 Regensburg, Federal Republic of Germany.

¹F. Cerdeira and M. Cardona, Phys. Rev. B **5**, 1440 (1972).

²F. Cerdeira, T. A. Fjeldly, and M. Cardona, Phys. Rev. B **8**, 4734 (1973).

³M. Balkanski, K. P. Jain, R. Beserman, and M. Jouanne, Phys. Rev. B **12**, 4328 (1975).

⁴M. Jouanne, R. Beserman, I. Ipatova, and A. Subashiev, Solid State Commun. **16**, 1047 (1975).

⁵M. Chandrasekhar, J. B. Renucci, and M. Cardona, Phys. Rev. B **17**, 1623 (1978).

⁶K. Jain, Shui Lai, and M. V. Klein, Phys. Rev. B **13**, 5448 (1976); to our knowledge this is the first experimental work on electronic Raman scattering in *p*-doped Si, which shows a single-particle spectrum.

⁷M. Chandrasekhar, M. Cardona, and E. O. Kane, Phys. Rev. B **16**, 3579 (1977).

⁸M. Chandrasekhar, U. Rössler, and M. Cardona, in *Proceedings of the Fourteenth International Conference on the Physics of Semiconductors, Edinburgh, 1978*, edited by B. L. H. Wilson (The Institute of Physics, Bristol, 1979), p. 961.

⁹P. M. Platzman, Phys. Rev. **139A**, 379 (1965).

¹⁰P. A. Wolff, Phys. Rev. **171**, 436 (1968).

¹¹H. Vogelmann and T. A. Fjeldly, Rev. Sci. Instrum. **45**, 309 (1974).

¹²S. M. Sze, *Physics of Semiconductor Devices* (Wiley-Interscience, New York, 1969).

¹³M. V. Klein, in *Light Scattering in Solids*, Topics in Applied Physics, edited by M. Cardona (Springer, New York, 1975), Vol. 8, pp. 148-207.

¹⁴P. M. Platzman and P. A. Wolff, *Waves and Interactions in Solid State Plasmas*, Solid State Physics (Academic, New York, 1973), Suppl. 13.

¹⁵D. C. Hamilton and A. L. McWorther, in *Light Scattering Spectra of Solids*, edited by G. B. Wright (Springer, New York, 1969), p. 309.

¹⁶S. S. Jha, Nuovo Cimento **63B**, 331 (1969).

¹⁷D. L. Mills, R. F. Wallis, and E. Burstein, in *Proceedings of the Second International Conference on Light Scattering in Solids, Paris 1971*, edited by M. Balkanski (Flammarion, Paris, 1971), p. 107; E. Burstein, D. L. Mills, and R. F. Wallis, Phys. Rev. B **4**, 2429 (1971).

¹⁸J. M. Luttinger, Phys. Rev. **102**, 1030 (1956).

¹⁹J. C. Hensel, private communication.

²⁰R. Loudon, Adv. Phys. **13**, 423 (1964).

²¹In a preliminary calculation (Ref. 8) we assumed for the central region the same number of carriers in the heavy and light hole bands. Thus a lower intensity ratio was calculated.

²²M. Grimsditch and M. Cardona, in *Proceedings of the Fourteenth International Conference on the Physics of Semiconductors, Edinburgh 1978*, edited by B. L. H. Wilson (The Institute of Physics, Bristol, 1979), p. 639.

²³M. Cardona and F. H. Pollak, Phys. Rev. **142**, 530 (1966); P. Lawaetz, Phys. Rev. B **4**, 3460 (1971).

²⁴D. Guidotti, Shui Lai, M. V. Klein, and J. P. Wolfe, Phys. Rev. Lett. **43**, 1950 (1979).